

Submitted to The Astrophysical Journal

An Adaptive Hierarchical Particle-Mesh Code With Isolated Boundary Conditions

Sergio Gelato

SISSA, via Beirut 2–4, I–34013 Trieste, Italy

David F. Chernoff and Ira Wasserman

Center for Radiophysics and Space Research, Cornell University, Ithaca NY 14853–6801,
USA

ABSTRACT

This article describes a new, fully adaptive Particle-Multiple-Mesh (PM²) numerical simulation code developed primarily for cosmological applications. The code integrates the equations of motion of a set of particles subject to their mutual gravitational interaction and to an optional, arbitrary external field. The interactions between particles are computed using a hierarchy of nested grids constructed anew at each integration step to enhance the spatial resolution in high-density regions of interest. As the code is aimed at simulations of relatively small volumes of space (not much larger than a single group of galaxies) with independent control over the external tidal fields, significant effort has gone into supporting isolated boundary conditions at the top grid level. This makes our method also applicable to non-cosmological problems, at the cost of some complications which we discuss. We point out the implications of some differences between our approach and those of other authors of similar codes, in particular with respect to the handling of the interface between regions of different spatial resolution. We present a selection of tests performed to verify the correctness and performance of our implementation. The conclusion suggests possible further improvements in the areas of independent time steps and particle softening lengths.

Subject headings: methods: numerical

1. Introduction

Ideally, a good cosmological N -body simulation should resolve in some detail the internal structure of individual galaxies (on mass scales as low as 10^6 to $10^7 M_\odot$ and on length scales of a few kiloparsecs or less) while at the same time representing the growth of density perturbations on the scale of clusters and even superclusters of galaxies. Galaxy morphologies are observed to correlate with their membership in clusters. The Virgo cluster is estimated to be an appreciable, if not dominant, source of tides on the Local Group 15 to 20 Mpc away. And when studying the nonlinear growth of galaxy-sized perturbations, one should not discount the possible coupling to modes with wavelengths as large as 50 Mpc (Gelb & Bertschinger 1994).

Achieving the required dynamic range is a difficult task given the limitations of present-day computers. Generally, numerical codes have been able to obtain a large dynamic range either in mass or in length, but not in both. Particle-particle (PP) methods (Aarseth 1985) and tree codes (Appel 1981, 1985; Barnes & Hut 1986; Jernigan & Porter 1989) have essentially unlimited length resolution, bounded only by the need to soften two-body encounters when modeling a collisionless physical system, but their use for simulations with more than a few tens, respectively hundreds, of thousands of particles is currently restricted to special-purpose hardware (such as GRAPE chips) or massively parallel computers (Dubinski 1996). Particle-mesh (PM) methods (Hockney & Eastwood 1981, hereafter HE; Efstathiou et al. 1985), by contrast, can integrate the orbits of millions of interacting particles even on a more modest single-processor mainframe or high-end workstation. The forces are computed by solving Poisson’s equation on a Cartesian grid. Barring complications such as a memory latency that increases with problem size, the computational cost per time step is linear in the number of particles and of order $N \log N$ in the number of grid cells (which is typically of the same order as the number of particles). The dynamic range in length, however, is limited by the maximum size of the grid, typically 256 or 512 cells on a side in three dimensions on a current single-processor computer. Parallel processing can naturally push this limit towards higher values.

One can circumvent this obstacle by decomposing the inter-particle forces into a long-range part, calculated by the PM technique, and a small-range part which can be evaluated in a number of different ways. For some time, a popular approach has been to compute the short-range forces by direct summation over all sufficiently close pairs of particles. This technique, known as the particle-particle, particle-mesh (P^3M) method (HE §8), was originally applied to plasma simulations where the electrostatic repulsion between charges of the same sign makes it difficult for large density contrasts to develop. Its use with gravitating systems suffers from the tendency for ever more particles to condense into small volumes, causing

the cost of the PP summation to become prohibitive as the system evolves. Increasing the total number of particles and resolving smaller scales (on which density perturbations become nonlinear at earlier times, at least in the presently favored “bottom-up” scenario) both exacerbate the problem. We are unaware of any P^3M simulations using more than about 5×10^5 particles. One may be able to raise this limit by using a tree method to compute the short-range forces, as in Xu’s (1995) TPM, but in principle the difficulty remains.

Most other attempts to enhance the spatial resolution of PM codes rely on the introduction of local grid refinements. This idea lies at the root of Couchman’s (1991) adaptive P^3M (AP^3M) (which however still uses direct summation where the number of particles is small enough), of numerous hierarchical PM codes (Chan et al. 1986; Villumsen 1989; Bien, Fuchs, & Wielen 1991; Anninos, Norman & Clarke 1994, hereafter ANC; Gelato, Chernoff, & Wasserman 1994; Jessop, Duncan & Chau 1994, hereafter JDC; Splinter 1996) and of various related approaches (James & Weeks 1986; Suisalu & Saar 1995a).

As pointed out by various authors, and most recently by Suisalu and Saar (1995b), the choice between PM, P^3M , and tree codes is not only a question of the spatial and mass resolution that can be achieved, but also of the behavior of each method with respect to two-body gravitational collisions. These are to be avoided when the physical system being modeled is essentially collisionless, as is the case for example for cosmological dark matter. PM codes usually prove to be less collisional, although it should be emphasized that this is at least in part a consequence of their spatial resolution being weaker than their mass resolution, and need not carry over to hierarchical PM methods unless precautions are taken to ensure that the mass granularity remains adequate at all times.

The purpose of this article is to document in some detail our implementation of a dynamically adaptive multiple-mesh code and the tests we performed to validate it. So far, only a brief report of an earlier stage of development (Gelato, Chernoff, & Wasserman 1994) and a description of the methodology but not of the tests (Gelato 1995) have appeared. Our code, like that of JDC, is able to track the formation and subsequent motion of density concentrations by dynamically adjusting the number, nesting depth and location of the subgrids. In our case, the entire grid structure is chosen afresh on every step. Since our first intended application was a cosmological problem—the formation of the Local Group—that requires the freedom to specify external tidal fields other than would be implied by periodic image charges, our code presents the relatively uncommon combination of an expanding system of coordinates with isolating (more properly non-periodic) boundary conditions. This introduces a number of complications not usually discussed in the literature on PM codes, and of which we shall give an account here. (Our method is also applicable to non-cosmological problems, for which isolating boundary conditions are an asset and the aforementioned com-

plications do not arise.) A future article (Gelato, Chernoff, & Wasserman 1996) will detail the results of our simulations of group formation.

The general outline of this paper is as follows. Section 2 describes in detail the method used. The tests and their results are presented in section 3. We conclude, in section 4, with our assessment of the strengths and limitations of this code.

2. Description of the method

2.1. Equations of motion

Our code integrates the equations of motion for a set of gravitating particles. These equations can be derived from the Lagrangian

$$\mathcal{L} = \frac{1}{2} \sum_i m_i |\dot{\mathbf{r}}_i|^2 + \frac{1}{2} \sum_i \sum_{j \neq i} m_i m_j V(\mathbf{r}_i, \mathbf{r}_j; t) + \frac{1}{2} \frac{\Lambda}{3} \sum_i m_i |\mathbf{r}_i|^2 - \sum_i m_i \Phi_x(\mathbf{r}_i; t). \quad (1)$$

Here the indices i and j span the set of particles in the system, m_i is the mass of particle i , $\mathbf{r}_i(t)$ its position at time t , and $V(\mathbf{r}, \mathbf{r}'; t)$ describes the law of pairwise interaction between particles. Ideally $V(\mathbf{r}, \mathbf{r}'; t) = 1/|\mathbf{r} - \mathbf{r}'|$ (we choose units such that $G = 1$) but the numerical method forces us to use an approximation which, due to adaptive grid refinement, can depend explicitly on time and on the individual coordinates \mathbf{r} and \mathbf{r}' , not just on their difference.

We could have included the term proportional to Λ (where Λ is an arbitrary constant) within the external potential Φ_x , but for cosmological applications it is useful to show it explicitly.

2.2. Expanding coordinates

It is often convenient to apply a time-dependent rescaling of the coordinate system, with new coordinates \mathbf{x} defined by $\mathbf{r} = a(t)\mathbf{x}$. An equivalent Lagrangian is then

$$\mathcal{L} = \frac{1}{2} a^2 \sum_i m_i |\dot{\mathbf{x}}_i|^2 + \frac{1}{2} a^2 \left(\frac{\Lambda}{3} - \frac{\ddot{a}}{a} \right) \sum_i m_i |\mathbf{x}_i|^2 + \frac{1}{2} \sum_i \sum_{j \neq i} m_i m_j V(\mathbf{x}_i, \mathbf{x}_j; t) - \sum_i m_i \Phi_x(\mathbf{x}_i; t). \quad (2)$$

For notational convenience, we define

$$H \equiv \frac{\dot{a}}{a} \quad (3)$$

$$\bar{\rho} \equiv \frac{3}{4\pi} \left(\frac{\Lambda}{3} - \frac{\ddot{a}}{a} \right). \quad (4)$$

Note that in principle $a(t)$ is arbitrary, reflecting our freedom to choose the coordinate system. For cosmological applications one normally chooses $a(t)$ to be the solution of Friedman's equation for some cosmological model, in which case $\bar{\rho}(t)$ is the background density and $H(t)$ the Hubble constant for that model. Later in this paper we shall impose the additional restriction $\bar{\rho}a^3 = \text{constant}$, which holds for cosmological models in the matter-dominated era.

The second term in the Lagrangian (2) can be regarded as involving an effective potential

$$\Phi_a(\mathbf{x}; t) = -\frac{1}{2}a^2|\mathbf{x}|^2\left(\frac{\Lambda}{3} - \frac{\ddot{a}}{a}\right) = -\frac{2\pi}{3}\bar{\rho}a^2|\mathbf{x}|^2, \quad (5)$$

which satisfies $\nabla^2\Phi_a = -4\pi\bar{\rho}a^2$. Similarly, in the continuum limit and for a Coulomb interaction ($V(\mathbf{x}, \mathbf{x}'; t) = a^{-1}(t)|\mathbf{x} - \mathbf{x}'|^{-1}$), the third term satisfies $\nabla_2^2 \sum_j m_j V(\mathbf{x}_i, \mathbf{x}_j; t) = -4\pi\rho(\mathbf{x}_i)a^2$, where the proper density ρ is given by $\rho(\mathbf{x})a^3 = \sum_j m_j\delta(\mathbf{x} - \mathbf{x}_j)$ and ∇_1 (respectively ∇_2) denotes differentiation with respect to the first (respectively the second) of the two position vectors on which V depends.

The usual derivation of the equations of motion from the Lagrangian (2) yields:

$$\ddot{\mathbf{x}}_i + 2H\dot{\mathbf{x}}_i = \frac{4\pi}{3}\bar{\rho}\mathbf{x}_i + a^{-2}\sum_{j \neq i} m_j \nabla_1 V(\mathbf{x}_i, \mathbf{x}_j; t) - a^{-2}\nabla\Phi_x(\mathbf{x}_i; t). \quad (6)$$

For later convenience, we define

$$\mathbf{f}_i = \frac{4\pi}{3}\bar{\rho}a^3\mathbf{x}_i + a\sum_{j \neq i} m_j \nabla_1 V(\mathbf{x}_i, \mathbf{x}_j; t) - a\nabla\Phi_x(\mathbf{x}_i; t). \quad (7)$$

This allows the equation of motion (6) to be written more compactly as

$$\ddot{\mathbf{x}}_i + 2H\dot{\mathbf{x}}_i = a^{-3}\mathbf{f}_i. \quad (8)$$

It is also useful to recast the equation in terms of a generalized time coordinate $\tau(t)$:

$$\frac{d^2\mathbf{x}_i}{d\tau^2} + 2A(\tau)\frac{d\mathbf{x}_i}{d\tau} = B(\tau)\mathbf{f}_i \quad (9)$$

with

$$A(\tau) \equiv \frac{1}{2}\left(\frac{dt}{d\tau}\right)^2\left(\frac{d^2\tau}{dt^2} + 2H\frac{d\tau}{dt}\right) \quad (10)$$

$$B(\tau) \equiv \frac{1}{a^3}\left(\frac{dt}{d\tau}\right)^2. \quad (11)$$

A common choice is the so-called conformal time, $d\tau = a^{-1}dt$; another (Efstathiou et al. 1985) is $\tau = a^\alpha$ for some constant α . Naturally, any sufficiently differentiable monotonic function of t is acceptable, and one is free to construct such a function *ad hoc* for each individual simulation. We avail ourselves of this freedom.

2.3. The top grid

We lay down a rectangular grid of N_x by N_y by N_z nodes with uniform spacings h_x , h_y and h_z . The values of N_x , N_y and N_z must be acceptable to the Fast Fourier Transform (FFT) routines used. (All our tests were done with $N_x = N_y = N_z$ a power of 2, and with $h_x = h_y = h_z$, as this is the most common situation in practice and the only one we needed for our applications.) At every step, a density is assigned to each grid point using the cloud-in-cell (CIC) algorithm. FFTs are then used to solve for the potential on the same grid, and an acceleration is obtained for each particle by differentiating the grid potential, then using CIC interpolation. We use a two-point finite-difference formula to compute the derivatives of the potential at grid nodes. This choice means that truncation errors in the force law scale with the square of the grid spacing (HE, §5-4).

The discrete Green’s function we use is obtained by sampling $1/|\mathbf{x} - \mathbf{x}'|$ at grid points (and Fourier transforming the result). This differs from the more common approach in cosmological PM codes (Efstathiou et al. 1985, Villumsen 1989) of basing the Green’s function on the seven-point finite difference approximation to the Laplacian; our choice has the merit of guaranteeing the truncation of the interaction law at large separations, as required for a correct implementation of isolated boundary conditions (Eastwood & Brownrigg 1979). Unlike in the P³M method, where the grid-based part of the force must possess a good degree of translational invariance to avoid introducing terms in the direct particle-particle contribution that depend explicitly on the position of each pair relative to the grid, we are not compelled to soften the interaction at small scales. To do so would cost us precious spatial resolution; already with our choice of Green’s function the effective force turns out to be softened at separations $\lesssim 2.5$ grid cells. A consequence of our decision not to soften the force law any further is that the Q -minimization procedure of HE §8-3-3, which requires the reference force to have no harmonics on scales smaller than the grid spacing, is not appropriate for us. The choice of the shape of the interaction law at small separations and of the charge assignment and force interpolation scheme is a matter of compromise between accuracy and computational cost. Our choices could undoubtedly be improved upon, but we preferred to concentrate our efforts on the more innovative aspects of our method.

2.4. Boundary conditions

Isolated boundary conditions are implemented by conceptually doubling the size of the grid in each dimension, and padding the density array with an appropriate constant value (normally zero) outside the principal octant, which contains the particles (HE, §6-5-4). If the Green’s function is truncated so that the interaction falls to zero at separations larger

than the system (before doubling), this completely suppresses any interaction between the system and its periodic images. The computed potential, however, will only match that of an isolated system within the principal octant (node indices 0 through $N_x - 1$, and similarly in the other two dimensions). Since we need to apply a gradient operator to the potential in order to compute the forces, there is a layer (one cell thick for our approximation to the gradient) in which we would not be able to compute them. We therefore restrict particles to lie in the region $1 \leq x/h_x \leq N_x - 2$, $1 \leq y/h_y \leq N_y - 2$, $1 \leq z/h_z \leq N_z - 2$. We do not use James' (1977) method to impose isolated boundary conditions without doubling the grid by calculating appropriate screening charges on the surface, since strictly speaking the procedure is only justified when the seven-point finite-difference approximation to the Laplacian is used in solving Poisson's equation. The FFT technique does not satisfy this condition.

In cosmological applications, the space surrounding the system is not to be thought of as empty, but rather as containing a background of uniform density ρ_b . (Departures from uniformity can be represented through an appropriate choice for the tidal potential Φ_x .) We must therefore add this background, convolved with the same (CIC) charge assignment function that is used for the particles. Its contribution to the density at any node on the boundary of the region where particles are allowed is then proportional to the number of cells adjacent to this node that lie outside the particle region: $\rho_b/2$ for nodes on a face, $3\rho_b/4$ on an edge, $7\rho_b/8$ at a vertex.

We implement the $(4\pi/3)\bar{\rho}\mathbf{x}$ term of the equation of motion (equation 6) by subtracting $\bar{\rho}$ from the density at all points before solving for the potential. If $\bar{\rho}$ coincides with the background cosmological density, the source function for the potential outside the principal octant is exactly zero. This is the most common case, and the one that presents the fewest conceptual and practical difficulties. With periodic boundary conditions it would also be the only possible case since the mean density outside the simulation box must always equal that inside it. With isolated conditions a mismatch is permissible, and could be used for example in applying an expanding or contracting grid to follow the evolution of an isolated system without a cosmological density background. The varying $a(t)$ would then be adjusted to match the expansion or contraction of the simulated system, providing better resolution at lower cost during the collapse phase.

A very significant difference between periodic and isolated boundary conditions is that the latter allow the exchange of mass, momentum, energy, angular momentum between the particles and the exterior. With periodic boundary conditions, there is effectively no exterior. Particle flows are a significant concern in cosmological applications, where matter may both leave and enter the computational box during the simulation. In a typical cosmological

model, the mass variance is of order unity in a sphere of radius $r_8 = 8h^{-1}$ Mpc. One expects particles at the edge of a sphere of radius r_8 to be displaced with respect to the center of mass of the sphere by about $r_8/3$, a significant length when compared to the size of a group or cluster of galaxies. A simulation of characteristic size r_8 may reasonably be expected to exhibit a twofold increase or decrease in the total mass within the box during a run. On smaller scales the variance is even larger, at least for the currently fashionable “bottom-up” scenarios of structure formation.

Exiting particles are easily handled by removing them from the simulation, but incoming particles have to be injected according to some prescription that fits the physical problem at hand. In the cosmological case, as long as the density perturbations grow linearly on the scale of the box, a reasonable prescription can be based on extrapolations from the linear theory. At late times, in the strongly non-linear regime, simply extrapolating from the linear solution causes large amounts of material to be injected which in reality would collapse into bound objects outside the box and remain outside. In other words, the Zel'dovich approximation is clearly inappropriate beyond the time at which caustics form. It would lead to a gross overestimate of the total mass flow into the box. An adequate model of the inflow in the nonlinear regime therefore requires an actual simulation of the mass flows in a larger region. This has become normal practice in simulations with tree codes, and hierarchical grid methods such as ours also lend themselves well to this approach. The main difficulty is that in order to keep the total number of particles manageable, one must essentially run a preliminary simulation simply to find out where the mass that flows into the region of interest originated and sample it with a finer granularity in the initial conditions. This may lead to problems of contamination by more massive “background” particles if the small-scale structure that is not resolved by the preliminary simulation turns out to have a significant impact on the dynamics. Furthermore, the presence of particles of different masses in the system could lead to spurious mass segregation effects. For these reasons, we attempted to keep the overall size of the computational box as small as possible, handling the tidal fields on larger scales, as well as any mass flows (as long as they remained moderate) as externally imposed boundary conditions.

This turned out not to be a particularly successful design choice, and we cannot recommend it to others. Injecting too many, or too few, particles can have a destabilizing effect. The first term on the right hand side of equation 6 has, in the usual case $\bar{\rho} \geq 0$, the effect of accelerating particles towards the boundary of the box. This is balanced by the second term, which represents the attraction between the gravitating particles. If more particles leave the box than are injected, the first term will tend to dominate and cause even more particles to be ejected; conversely, if too many particles are added the material will tend to collapse towards the center. This may be taken to represent a physical effect: a void is expected

to expand faster than the universal average, an over-density more slowly. But unless the algorithm for replenishing the box with particles is well thought out, a runaway instability may occur. In practice we have found it expedient to couple the injection of particles to the outflow so as to maintain a constant mass within the system. We then monitor the cumulative mass of particles so recycled and compare it with the total mass in the box. If the ratio becomes too large (greater than 10% or so), we take it as an indication that one needs to simulate a larger volume of space. As the volume that needs to be simulated grows larger, our original motivation for using isolated boundary conditions becomes weaker. It turns out that the method we described in this paragraph works much better if the system is located in a region of lower density than the cosmic mean, as the mass fraction that undergoes re-injection is smaller in that case. This allows us to simulate a number of interesting systems, but is not suitable for statistical studies involving a random selection of initial conditions.

Momentum, angular momentum, and energy can be carried by the particles that flow in and out of the system and by direct interaction with the external potential $\Phi_x(\mathbf{x}; t)$ and the uniform density we impose in the space that surrounds the particle region. The latter unfortunately has the cubic symmetry of the computational box rather than the more convenient spherical symmetry that would be required for an exact cancellation of the induced tides. Consequently, these tides are always present except in the pure non-cosmological case with a a constant, where the background density vanishes. Whether this is a serious drawback depends on the physical problem being studied. If necessary, one can enlarge the computational box (this may be required in any case to keep mass flows under check), include a compensating term in Φ_x , or both.

2.5. Introducing subgrids

The idea of adding subgrids in regions where better spatial resolution is required is not a new one. Past approaches have differed on whether to add mass resolution at the same time by splitting the particles into a larger number of less massive ones, on how to minimize errors at the interface between the finer and the coarser grid, and on whether the solution on the coarser grid should be modified to take into account the results from the finer grid.

2.5.1. Subgrids and particles

Unlike Villumsen (1989) and Splinter (1996), we do not automatically introduce a new set of less massive particles on each subgrid. We take the view that our initial mass gran-

ularity already matches the resolution we wish to achieve, and simply increase the force resolution (by adding subgrids) when and where the particle density is high enough to make this permissible and worthwhile. This allows the decision of where to place subgrids to be made on a step by step basis, and spares us the need to perform a first simulation without subgrids to find out where particles of smaller mass should be placed in the initial conditions. An additional advantage of having a single set of particles of equal mass is that we need not worry about mass segregation effects. A drawback is that maintaining equivalent resolution within a larger computational volume requires more particles. Of course our code does support multiple particle masses, and as will become clear below the criteria for subgrid placement can be tuned to favor tracking the lower-mass particles; we may therefore decide to experiment with particles of different masses in future.

In our scheme the various grids are merely devices, introduced independently on each integration step, to compute inter-particle forces. In this respect we are closer in spirit to Couchman’s AP³M than to most other multiple-grid approaches. Ours is effectively (in the terminology of ANC) a Particle-Multiple-Mesh (PM²) scheme. This distinction will have important consequences below. Since there is only one set of particles that exist independently of any subgrids, the equivalent of a back-reaction from the subgrid solution to the parent grid is automatically included: it is mediated by the particles themselves.

We typically decrease the grid spacing by a factor of two for each additional level of subgrids. Each subgrid thus covers a substantial number of cells of its parent grid. Other integral refinement factors are allowed by our formulation (subject to the condition that the boundaries of any subgrid must coincide with cell boundaries of the parent grid) but become increasingly inefficient in terms of volume coverage and we have not tried them in practice. They would also exacerbate any “ringing” at the interface between a subgrid and its parent grid; since this is one of the most delicate aspects of any hierarchical grid scheme, it is probably not advisable to use refinement factors larger than two under any circumstances.

A particle passing from a region of low resolution to one of higher resolution effectively undergoes a sudden change in its spatial extent. (In PM codes, particles are best thought of as extending over about one grid cell or more, depending on the shape of the interaction law and on the charge assignment scheme.) In its current state, our code takes no particular precautions against any transients that may result. Our comparison tests between runs that use adaptive subgridding and runs with uniform resolution show that such transients are not important enough to produce significant discrepancies in the results. This is fortunate, since otherwise we would have had to associate a time-dependent smoothing length with every particle, which would complicate the method. That the smoothing length would have to be associated with the particle rather than with the location relative to a subgrid follows both

from our choice to treat the particles as primary and the grids as auxiliary objects and from the fact that new subgrids may be added, removed or relocated to follow the flow at every step.

2.5.2. Forces on subgrids

Our strategy for computing the forces between subgrid particles differs slightly from that of Villumsen. His approach was to recalculate the potential on the entire parent grid after having set the density in the volume occupied by the subgrid to a constant value equal to the mean density within the subgrid, and use this solution as the tidal field on the subgrid particles from the rest of the system. The forces between subgrid particles were then computed in the usual way by solving for the potential on the subgrid. Instead, we first compute forces for all particles on the parent grid, then generate the density array on the subgrid (whose nodes must be aligned with those of the parent grid) as well as on a coarser grid that has the same spacing as the parent grid and nodes in the same locations but covers only the volume of the subgrid. Since coordinates on the subgrid are affected by the same expansion factor $a(t)$ as on the parent grid, we must subtract the same $\bar{\rho}$. We solve for the forces on all subgrid particles from both these density arrays, and add the difference to the forces we had previously calculated on the parent grid. This avoids double counting and means in effect that pairwise forces between particles that both lie in the subgrid are always evaluated at the higher of the two resolutions. The coarse FFT on the subgrid involves far fewer grid points, so our approach is more efficient than Villumsen's. It is also more flexible, in that we only need to store the accumulated force for every particle and the density potential for a single subgrid at a time, independently of the number and nesting depth of subgrids. The cost of actually storing a force vector for every particle may seem high when one knows that in a traditional PM code with leapfrog time stepping the particle accelerations can be interpolated when the velocities are updated and need not be kept afterwards; but saving them allows us to use them to adjust the time step and to compute subgrid corrections to the energy conservation test. On the other hand, we could have supported independent time steps had we chosen to save the potential on each subgrid instead. This, however, would have caused the storage requirements to scale with the subgrid nesting depth.

Let S be the set of particles in the subgrid, C its complement. Schematically, the acceleration on particle i is computed as follows. For $i \in C$,

$$\mathbf{F} = \sum_{j \in C \cup S} m_j \nabla_1 V_P(\mathbf{x}_i, \mathbf{x}_j). \quad (12a)$$

For $i \in S$,

$$\begin{aligned} \mathbf{F} = & \sum_{j \in C} m_j \nabla_1 V_P(\mathbf{x}_i, \mathbf{x}_j) + \sum_{j \in S} m_j \nabla_1 V_P(\mathbf{x}_i, \mathbf{x}_j) \\ & + \sum_{j \in S} m_j \nabla_1 V_S(\mathbf{x}_i, \mathbf{x}_j) - \sum_{j \in S} m_j \nabla_1 V_{P'}(\mathbf{x}_i, \mathbf{x}_j) \end{aligned} \quad (12b)$$

where V_P is the approximation to the Coulomb potential on the parent grid, V_S the approximation on the subgrid, and $V_{P'}$ that on the subset of the parent grid that covers the subgrid. (In reality, the sums are evaluated by FFT and include the $\bar{\rho}$ term.) $V_P = V_{P'}$ to a very good degree, provided only that the grid nodes are in the same locations. (This is an essential requirement: we have found that violating it has deleterious effects on the solution.) The two rightmost terms in the display of equation (12b) therefore cancel each other. Note that we add together force contributions from the various grids rather than the potentials; this allows the arbitrary additive constant in the potential to differ from grid to grid without affecting our solution.

2.5.3. Boundary conditions on subgrids

We impose isolated boundary conditions on the subgrid, with an external background density ($\bar{\rho}$) equal to that used on the parent grid. It may seem more appropriate to use the mean density within the subgrid, or—better yet—the mean density in the immediate vicinity of the subgrid; but one should note that some ringing is to be expected no matter what the exact scheme adopted since the density at the boundary of the subgrid always has some short-wavelength component that is resolved on the subgrid but not on the parent grid. The usual approach in codes of this type is to try to limit the ringing by introducing around the subgrid a buffer region, in which particles contribute to the potential but are not affected by it, and/or a transition region in which the potentials of the parent grid and of the subgrid are blended linearly. The transition region implements the variable smoothing length we alluded to at the end of the previous subsection. As already noted, it is of limited usefulness in our case since it doesn't guard against transients induced by the sudden activation of a new subgrid. The possible motivation for introducing a buffer region can be understood by considering the case of a particle P_0 located on the subgrid but near its edge, and subject to the forces of two nearby equidistant particles P_S , also on the subgrid, and P_B just outside it. In the exact solution, P_S and P_B exert forces of equal magnitude on P_0 . Without a buffer region, the calculated force from P_S is stronger. This can create spurious small-wavelength perturbations as the pair (P_0, P_S) tends to collapse on its own rather than as a triplet (P_S, P_0, P_B) . The introduction of a buffer region would allow the balance to be preserved between the attractions of P_S and P_B .

Our implementation of the buffer region is as follows. Extending the notation introduced in the previous subsection, we have split C into the buffer region B and a distant exterior X . Equation 12b is modified in that the sum over $j \in C$ becomes a sum over $j \in X$ and the sums over $j \in S$ become sums over $j \in (S \cup B)$. We normally set the thickness of this buffer region to be equivalent to three cells of the parent grid: the grid-based force does not differ significantly from the exact Coulomb force at separations this large, so that $V_S \simeq V_P$. Since the thickness of the buffer region is fixed in units of the spacing of the parent grid, large refinement factors result in the buffer region “eating away” most of the volume of the subgrid. This is one of the reasons why we only experimented with a refinement factor of 2 at each level.

2.5.4. *Adjacent subgrids*

An essential feature of this buffer region is that it enables us to use multiple adjacent subgrids to cover extended structures that are worthy of higher resolution but do not fit within a single grid. This could occur either because of their size or because they are located too close to other high-density objects already covered by their own subgrids. (We do not allow arbitrary overlap of subgrids, for both simplicity and efficiency.) A problem that might arise when the boundary between two adjacent subgrids cuts through the middle of a high density structure is that the force between two nearby particles separated by the boundary would be calculated with the (poorer) resolution of the parent grid. Thanks to the buffer region around each subgrid, this difficulty is avoided: the force exerted by either particle on the other will be computed at subgrid resolution by virtue of each particle lying in the buffer region of the other’s subgrid.

In the overlap region between adjacent subgrids, it matters little whether the border region is implemented as described above or in the following alternative way, by subjecting particles in B to the subgrid forces without including them in the subgrid potential. This corresponds to applying equation 12a to particles $i \in X$ only, and equation 12b to particles $i \in (S \cup B)$. Our first implementation used the latter approach, and comparison tests show only minute differences between the results of both variants.

A difficulty arises wherever the buffer region has finite width and does not overlap with an adjacent subgrid. Then the balancing of the forces by P_S and P_B over P_0 comes at the cost of a violation of Newton’s second law: the force exerted by P_0 on P_B , being computed on the parent grid, does not balance the force by P_B on P_0 . The net result is that P_B will be accelerated outwards, away from the subgrid. (If the alternative implementation of the buffer region is adopted, the net effect has opposite sign and tends to push the particles inwards.)

The consequences for the orbit of a bound clump can be spectacular, as the following worst-case example, illustrated by figure 1, shows. We launch a 4096-particle realization of a truncated isothermal sphere (with a half-mass radius of 0.02 units, corresponding roughly to half the cell width on the top grid) with a mean velocity of 0.1 units towards a region covered by a fixed subgrid (the inner bounds of which are indicated by dotted lines in the figure) with refinement factor of two and a buffer region of width 0 (solid curve) or 2 (dashed curve) parent grid cells. For this example we adopted the alternative implementation of the buffer region, which causes the particles to be accelerated inwards. The initial velocity is along the x axis, perpendicular to the faces of the subgrid. The figure shows the x coordinate of the center of mass of the sphere as a function of time t . When the buffer region is suppressed (width 0, solid curve) the clump enters and exits the subgrid without changes to its bulk velocity. (The apparent turnaround occurs when the clump reaches the edge of the computational volume and some particles leave the box. The solid curve reflects the mean velocity of only those particles that remain in the box.) The presence of a finite buffer region, by contrast, causes the clump to accelerate as it enters the subgrid, and to bounce back as it tries to exit on the other side. The reason it doesn't simply lose the momentum it gained when entering the subgrid is that the momentum change depends on the difference between the forces calculated on the subgrid and on the parent grid, and that the passage through the more highly resolved subgrid has allowed the clump core to relax to a more sharply peaked density profile, increasing the force mismatch. The main features of this behavior are quite generic: a more carefully constructed clump with a larger number of particles that was allowed to settle into a numerical equilibrium before being launched through the subgrid underwent similar, if slightly milder, accelerations and rebounds.

Clearly it is better for us to suppress the buffer region where there is no adjacent subgrid. The violation of momentum conservation that a finite border region implies can have a drastic influence on the orbit of a bound clump. This would not be much of a concern if we could guarantee that bound clumps are always entirely covered by subgrids at the same resolution; the problem does not arise for smooth distributions of matter where short-range forces don't predominate. (In section 3.3 we demonstrate this fact through a test of smooth infall onto a localized seed mass perturbation.) In principle, an adaptive algorithm for subgrid placement based on the density should tend to ensure this. However, one may want to place additional restrictions on which regions are followed at higher resolution, in which case the guarantee does not hold and we must take the precaution of suppressing the buffer region in the absence of an adjacent subgrid. Note that the problem is less severe when expanding coordinates are used, as in cosmological applications, since the peculiar velocity acquired while crossing a subgrid interface will be damped away.

Why has this same difficulty not been recognized by other authors, notably ANC and

Splinter (1996)? The reason may be traced to a fundamental difference in philosophy between our code and theirs. The very idea of a particle on a subgrid interacting symmetrically with a particle on the parent grid is a consequence of our decision to regard the particles, rather than the density field on the grids, as primary. In a scheme where every particle is associated with only one grid, and particularly when the dynamics of the parent grid particles are unaffected by the subgrid (the so-called “one-way interface” schemes), momentum conservation should be examined separately on each grid: on the parent grid, no violation is expected, while on the subgrid the effects of the parent grid particles are treated as an external field and the buffer and transition regions are used to smoothly bring any particles exiting the subgrid under the control of the parent grid field alone, as test particles, rather than reflecting them back into the subgrid. Thus, the apparent contradiction between these authors’ use of a buffer region two cells wide and our restriction of the buffer region to the sole case of adjacent subgrids does not signal an error either on our part or on theirs, but is merely a manifestation of our different view of the respective roles of particles and grids.

2.5.5. Subgrid placement algorithms

A distinguishing feature of our code is that the activation of subgrids is entirely automated: the user need only set a few parameters (maximum depth, and various optional thresholds), after which the code decides at every step where to place subgrids. Tuning the criteria for subgrid placement is not an easy task; our current choices can undoubtedly be improved upon. Here we shall describe some of the criteria we have implemented. Not all of them have proved very useful in practice.

Our subgrids have fixed shape and size, and may not overlap. Consequently, we found it simplest to introduce a uniform tiling of subgrids covering the entire volume of the parent grid. Each subgrid may be either active or inactive. A subgrid is activated whenever our requirements for subgridding are satisfied within its volume. We are free to choose the origin of the tiling independently for every parent grid at every step. We make use of this freedom to reduce the number of active subgrids. Typically we try eight different possible origins, and adopt one that requires the activation of fewest subgrids.

The first criterion for subgrid activation is that the particle number density be sufficiently high in at least part of the covered region: there is no point in the grid ever being much finer than the smallest distance between particles. To activate a subgrid, we require that among the corresponding cells of the parent grid either (a) at least one cell contains more than N_0 particles; or (b) one cell contains at least N_1 particles and its 26 immediate neighbors together contain a further $N_3 - N_1$ particles or more. N_0 , N_1 and N_3 are specified

as input parameters to the code.

The main reason for considering cubes of $3 \times 3 \times 3$ cells as well as single cells is that one needs to detect the collapse of a high-density region before it is too advanced: the additional resolution is already required during the later stages of collapse. We don't try to detect larger, lower-contrast potentially collapsing structures on larger scales since for separations larger than about three cells the forces are computed accurately on the parent grid.

One way of choosing N_1 and N_3 is the following. Let N_{eff} be a measure of the mean number of particles per cell in some larger region, such as the entire candidate subgrid. (This measure need not be unbiased; in fact, if the mean particle number density is very low we found it necessary to artificially increase N_{eff} by setting it to the value 1. Otherwise our subgrid placement criterion would be satisfied far too easily in low-density regions.) If the particle counts were distributed according to Poisson statistics, one would expect a group of n_c cells to contain on average $n_c N_{\text{eff}}$ particles, with a standard deviation $(n_c N_{\text{eff}})^{1/2}$ around that mean. By setting $N_1 = N_{\text{eff}} + N_\sigma N_{\text{eff}}^{1/2}$ and $N_3 = 3^3 N_{\text{eff}} + N_\sigma (3^3 N_{\text{eff}})^{1/2}$, where N_σ is a tunable parameter, we try to ensure that only particularly significant deviations from homogeneity trigger subgrid activation.

We have found that this approach works reasonably well during the early stages of nonlinear evolution, where it causes higher resolution to be applied to the regions we are most interested in. However, as the simulation progresses we have needed to increase N_σ in order to limit the proliferation of subgrids, as our goal was merely to achieve high resolution in a few large peaks near the center of the computational box. Clearly the criteria can and should be tuned according to the needs of individual applications; no single choice is optimal for all cases.

2.6. Time step selection

We follow the usual practice in PM codes of advancing the positions and velocities of the particles in leapfrog fashion:

$$\frac{d\mathbf{x}_i}{d\tau}(\tau + \delta\tau/2) = \left(\frac{1 - A(\tau)\delta\tau}{1 + A(\tau)\delta\tau} \right) \frac{d\mathbf{x}_i}{d\tau}(\tau - \delta\tau/2) + B(\tau)\delta\tau\mathbf{f}_i(\tau) \quad (13)$$

$$\mathbf{x}_i(\tau + \delta\tau) = \mathbf{x}_i(\tau) + \delta\tau \frac{d\mathbf{x}_i}{d\tau}(\tau). \quad (14)$$

An alternative formula applies on a starting step, when both the positions and the velocities are known at the same time τ :

$$\mathbf{x}_i(\tau + \delta\tau/2) = \mathbf{x}_i(\tau) + \frac{\delta\tau}{2} \left(1 - \frac{A(\tau)\delta\tau}{2} \right) \frac{d\mathbf{x}_i}{d\tau} + \frac{\delta\tau^2}{8} B(\tau) \mathbf{f}_i(\tau). \quad (15)$$

Likewise, one can synchronize positions and velocities at the final step by advancing the velocities from $\tau - \delta\tau/2$ to $\tau + \delta\tau/2$ then updating the positions as

$$\mathbf{x}_i(\tau + \delta\tau/2) = \mathbf{x}_i(\tau) + \frac{\delta\tau}{2} \left(1 + \frac{A(\tau)\delta\tau}{2} \right) \frac{d\mathbf{x}_i}{d\tau} - \frac{\delta\tau^2}{8} B(\tau) \mathbf{f}_i(\tau). \quad (16)$$

In large simulations, it is particularly important to avoid taking more time steps than required to obtain accurate results. The time step should therefore be allowed to vary. In the standard leapfrog formulation, the cancellation of second-order terms in equation (13) depends on A being evaluated at the midpoint of the velocity step. The cancellation of the second-order term in the formula to update the positions is less important since the \mathbf{f}_i are known; however, it contributes to lowering the operation count for the method. Various approaches can be used to change the time step in the middle of a simulation. One is to use a different midpoint in equation (13) and calculate the corresponding $A(\tau)$. The other, which is the one we adopted, is to keep $\delta\tau$ constant by an appropriate choice of the function $\tau(t)$. We construct this function and its first and second derivatives, which are needed to evaluate A and B according to equations (10) and (11), step by step as the simulation progresses. (In practice, we do not allow $d\tau/dt$ to vary too quickly, since that tends to spoil the results. We shrink δt by at most 25% on each step, and let it grow even more slowly. Situations in which this forces a larger δt than desired have fortunately been very rare in our runs.)

Our preferred criterion for determining the time step is the Courant condition:

$$\delta t \leq \varepsilon \min_j \frac{h_j}{|\dot{\mathbf{x}}_j|} \quad (17)$$

where the index j spans the set of all particles, h_j is the grid spacing of the finest grid used to compute the forces on particle j , and $\varepsilon < 0.5$ is a constant coefficient. $\dot{\mathbf{x}}_j$ should be taken as being the mean velocity over the time step, and is a function of both the velocity before the step is taken and of the acceleration. The latter can be important if the initial velocity is uncharacteristically small, for example when all the particles are initially at rest. The equation for the maximum acceptable δt for each particle is actually a quartic. We do not solve it exactly, preferring to estimate a close lower bound on the solution for the particles with the tightest δt constraints. This way of taking the accelerations into account fulfills the same function as other authors' use of the maximum density on a subgrid to estimate a local dynamical time.

In some cosmological simulations with a large number of particles, we found that adopting the smallest δt found in this fashion was leading to time steps much shorter than warranted by our physical understanding of the dynamical time scales involved (based on the maximum density). This turned out to be due to a small number of high velocity particles: the tail of the velocity distribution produced by the violent relaxation of a newly collapsed object, which is naturally better sampled as the number of particles in the simulation increases. Since these particles represent a small fraction of the mass in the typically high-density regions in which they are found, their motion has almost no impact on the mean gravitational field, which evolves on much longer time scales. This led us to modify the time step criterion for these simulations by pretending that the velocity of each particle before the time step is negligible and basing the choice of δt solely on the accelerations. This is not unreasonable for cosmological applications since in the linear regime the velocities and peculiar accelerations are related and in virialized clumps they are a better indication of the dynamical time scale than the velocity of the fastest particle (which is not the same as the local velocity dispersion). Moreover, expanding coordinates have the property that peculiar velocities are damped away and need to be continually regenerated by the forces. As a further precaution, we have analyzed the velocities of the particles at a late stage in a simulation run with this relaxed time step criterion and found, as intended, that the number of particles that violated the stricter Courant condition was small. The relaxed criterion is known to fail, however, for highly ordered collapse (such as that of a homogeneous sphere). In that case the largest acceleration does not provide a good estimate of the time scale over which the mean field evolves: based as it is on the more extended distribution at the beginning of the step, it systematically overestimates the maximum allowable time increment. Accordingly, we only resort to the relaxed criterion, with some reluctance, for runs in expanding coordinates, with large numbers of particles, and where different mass shells collapse at different times. Our tests on smaller cosmological runs have shown the results to be substantially identical, but with the relaxed condition requiring a much smaller number of steps.

We use a single value of δt for all particles on all subgrids at any given step. A far better approach in principle, but much more complicated to implement, would be to adopt multiple time steps and to distinguish between the time steps used for advancing individual particles and those for updating the potentials on subgrids. Independent time steps for the particles would require a way of estimating the accelerations at positions and times slightly different from those for which the potential has been calculated. For this, it may be necessary to calculate the time derivative of the subgrid potential as well as the potential itself. In addition to the constraints resulting from the rate of change of the subgrid density, the frequency with which the subgrid potential is recalculated can also be affected by particles flowing out of the region in which forces can be interpolated from the subgrid potential:

in our scheme, such events change the mapping between particles and subgrids and require recalculation of all the subgrid potentials involved if the total momentum is to be conserved. These are our main reasons for adopting a single time step for all grids. The other main reason is that a single time step allows us to process subgrids one by one, accumulating the force contributions on each particle without needing to store the solutions for the potential on many nested subgrids simultaneously. Almost any other time step scheme requires these subgrid potentials to be available simultaneously.

The coefficients in the leapfrog formulae (equations 13 and 14) can depend on time. For good accuracy, their variation in a time step must be small. This constraint is clearly unrelated to the grid spacing, and must be imposed separately. It is equivalent to the requirement that $|H\delta t| \ll 1$.

2.7. Conservation laws

Conservation laws provide an important diagnostic of how accurately the equations of motion have been integrated in a given simulation. Good conservation of physical invariants is not a sufficient condition for a good integration, but it is a necessary one.

In the absence of coordinate expansion, subgrids, and external fields, a PM code such as ours would be expected to conserve total momentum algebraically, energy a little less well, and angular momentum only in the limit where the interparticle separation is much larger than the grid spacing (HE §7–6).

2.7.1. Energy

Cosmic expansion causes the usual equation of conservation of the total energy, $E = T + W = \text{constant}$ (where T is the kinetic, W the potential energy), to be replaced with the Layzer-Irvine (Irvine 1961; Layzer 1963) equation, which can be derived from the well-known property of the Hamiltonian \mathcal{H} :

$$\frac{d\mathcal{H}}{dt} = \frac{\partial\mathcal{H}}{\partial t}. \quad (18)$$

Computing the canonical momentum from equation 2,

$$\mathbf{p}_i \equiv \frac{\partial\mathcal{L}}{\partial\dot{\mathbf{x}}_i} = m_i a^2 \dot{\mathbf{x}}_i, \quad (19)$$

it follows in the usual way that

$$\begin{aligned}\mathcal{H} &= \sum_i \mathbf{p}_i \cdot \dot{\mathbf{x}}_i - \mathcal{L} \\ &= \frac{1}{2} \sum_i \frac{|\mathbf{p}_i|^2}{m_i a^2} - \frac{2\pi}{3} \bar{\rho} a^2 \sum_i m_i |\mathbf{x}_i|^2 - \frac{1}{2} \sum_i \sum_{j \neq i} m_i m_j V(\mathbf{x}_i, \mathbf{x}_j; t) + \sum_i m_i \Phi_x(\mathbf{x}_i; t).\end{aligned}\quad (20)$$

We define the kinetic and potential energies as:

$$K \equiv a^2 T \equiv \frac{1}{2} \sum_i \frac{|\mathbf{p}_i|^2}{m_i a^2} \quad (21)$$

$$W \equiv -\frac{1}{2} a \sum_i \sum_{j \neq i} m_i m_j V(\mathbf{x}_i, \mathbf{x}_j; t) - \frac{2\pi}{3} a^2 \ddot{a} \sum_i m_i |\mathbf{x}_i|^2. \quad (22)$$

Then

$$\mathcal{H} = a^2 T + a^{-1} W + \sum_i m_i \Phi_x(\mathbf{x}_i; t). \quad (23)$$

Our exclusion of the external potential Φ_x from the definition of W is somewhat arbitrary. In practice, one wants to separate the terms associated with the mutual interactions of particles, which do measure the accuracy of the integrator, from the correction terms that merely account for known, external sources and sinks of energy.

In applying equation 18, one notes that in

$$\frac{\partial a^{-1} W}{\partial t} = -H a^{-1} W + a^{-1} \frac{\partial W}{\partial t} \quad (24)$$

the last term does not vanish if aV depends explicitly on time (as may occur in practice when a new subgrid is activated and the force resolution increases locally), or if $a^3 \bar{\rho}$ is not constant. For simplicity, we shall assume $a^3 \bar{\rho} = \text{constant}$ from now on, since that is the only case of actual practical interest to us.

Straightforward algebra leads to the two equations:

$$\frac{d}{dt} \left(a^3 T + W \right) + H a^3 T + a \sum_i m_i \dot{\mathbf{x}}_i \cdot \nabla \Phi_x(\mathbf{x}_i; t) + \frac{1}{2} \sum_i \sum_{j \neq i} m_i m_j \frac{\partial a V}{\partial t} = 0 \quad (25)$$

$$\frac{d}{dt} \left(a^4 T + a W \right) - H a W + a^2 \sum_i m_i \dot{\mathbf{x}}_i \cdot \nabla \Phi_x(\mathbf{x}_i; t) + \frac{1}{2} a \sum_i \sum_{j \neq i} m_i m_j \frac{\partial a V}{\partial t} = 0 \quad (26)$$

which although physically equivalent are evaluated numerically in slightly different ways when $a(t)$ is not constant.

The corresponding conserved quantities are:

$$\begin{aligned} C &= a^3 T + W + \int H a^3 T dt + \int a \sum_i m_i \dot{\mathbf{x}}_i \cdot \nabla \Phi_x(\mathbf{x}_i; t) dt \\ &+ \frac{1}{2} \int \sum_i \sum_{j \neq i} m_i m_j \frac{\partial a V}{\partial t}(\mathbf{x}_i, \mathbf{x}_j; t) dt \end{aligned} \quad (27)$$

$$\begin{aligned} C' &= a(a^3 T + W) - \int H a W dt + \int a^2 \sum_i m_i \dot{\mathbf{x}}_i \cdot \nabla \Phi_x(\mathbf{x}_i; t) dt \\ &+ \frac{1}{2} \int a \sum_i \sum_{j \neq i} m_i m_j \frac{\partial a V}{\partial t}(\mathbf{x}_i, \mathbf{x}_j; t) dt \end{aligned} \quad (28)$$

In proper-length coordinates ($a \equiv 1$), the first integral term ($+\int H a^3 T dt$ or $-\int H a W dt$) vanishes and both criteria reduce to the usual law of conservation of energy. The last two terms represent respectively the work done by external fields and time dependence in the interaction law. One may question the appropriateness of including the latter effect, since its origin lies in the numerical method used rather than in the underlying physics. Shouldn't contributions from the $\partial(aV)/\partial t$ term be counted as violations of energy conservation by the code? In reply we point out that much of that term may result from fluctuations in the zero level of the gravitational potential on subgrids, which we did not attempt to suppress since they have no bearing on the computed forces. And in any case the $\partial(aV)/\partial t$ contribution should be evaluated so that its magnitude relative to the other terms may be assessed.

It is unrealistic to expect a PM code to conserve C and C' arbitrarily well when gravitational instability causes the individual terms (W , $a^3 T$) to grow by orders of magnitude. Like many other authors before us, we deem C and C' adequately conserved if their variation is a small fraction (typically 1–3%) of the change in W or aW , respectively.

In our definition of W (equation 22) we excluded the self-energy terms $\sum_i m_i^2 V(\mathbf{x}_i, \mathbf{x}_i; t)$. But the natural way of calculating the potential in a PM code effectively includes these terms (the restriction $j \neq i$ can be ignored since the scheme avoids self-forces); we subtract them explicitly as part of our energy conservation test.

2.7.2. Momentum

We adopted a momentum-conserving scheme for calculating the forces. The total momentum should therefore be unaffected by particle-particle interactions on any given grid, and (given the precautions we have taken in our handling of the buffer region surrounding

each subgrid) be only weakly modified by interactions across the boundary between adjacent subgrids. However, it is still affected by all other interactions between particles and external fields, including the constant-density background outside the computational box. (This field gives rise to forces only when isolated boundary conditions are used, which is the reason why it isn't normally discussed in the literature.)

The canonical momentum \mathbf{p}_i of particle i satisfies

$$\dot{\mathbf{p}}_i = -\frac{\partial \mathcal{H}}{\partial \mathbf{x}_i} = \frac{4\pi}{3}\bar{\rho}a^2m_i\mathbf{x}_i + m_i \sum_{j \neq i} \nabla_1 V(\mathbf{x}_i, \mathbf{x}_j; t) - m_i \nabla \Phi_x(\mathbf{x}_i; t). \quad (29)$$

Summation over all particles and time integration yield a conserved quantity

$$\mathbf{P}_c = \sum_i \mathbf{p}_i - \frac{4\pi}{3} \int \bar{\rho}a^2 \sum_i m_i \mathbf{x}_i dt - \int \sum_i \sum_{j \neq i} m_i m_j \nabla_1 V(\mathbf{x}_i, \mathbf{x}_j; t) dt + \int \sum_i m_i \nabla \Phi_x(\mathbf{x}_i; t) dt. \quad (30)$$

In the special case when (i) Φ_x has no spatial dependence, (ii) $\sum_i m_i \mathbf{x}_i \equiv 0$ or $\bar{\rho} \equiv 0$, and (iii) $\nabla_1 V + \nabla_2 V \equiv 0$, the total momentum is constant. If one's aim is to measure the deviation of the results from those expected when $\nabla_1 V + \nabla_2 V \equiv 0$ (such a deviation can occur in the presence of subgrids), one should naturally omit the corresponding term from equation 30.

2.7.3. Angular momentum

Likewise, the conservation of angular momentum $\mathbf{J}_i \equiv \mathbf{x}_i \times \mathbf{p}_i$ amounts to the constancy of

$$\mathbf{J}_c = \sum_i \mathbf{J}_i - \int \sum_i \sum_{j \neq i} m_i m_j \mathbf{x}_i \times \nabla_1 V(\mathbf{x}_i, \mathbf{x}_j; t) dt + \int \sum_i m_i \mathbf{x}_i \times \nabla \Phi_x(\mathbf{x}_i; t) dt. \quad (31)$$

Angular momentum is only conserved if (i) $(\mathbf{x}_i \times \nabla_1 + \mathbf{x}_j \times \nabla_2)V \equiv 0$ and (ii) Φ_x is a function of $|\mathbf{x}|$ and t alone. The exact Coulomb force law satisfies the first condition, but grid-based approximations to it don't. As in the analogous case for the momentum, if the aim is to measure deviations from the ideal behavior where (i) is satisfied, then one should compare the magnitude of the corresponding term to $\sum_i \mathbf{J}_i$ itself, and to the magnitude of the external torque term when present.

3. Tests of the method

3.1. Force errors and subgrids

Our first tests are meant to see how accurately the code calculates the accelerations of particles given a known mass configuration. The simplest case is that of the forces due to a single point mass, which can be compared to the value predicted by Coulomb’s law. Figure 2 illustrates this comparison. It shows the accelerations induced by a single particle at the center of a 32^3 grid with isolated boundary conditions. A single 32^3 subgrid, twice as fine as the top grid, was centered on the massive particle. Two sets of points are readily distinguished, corresponding to test particles inside and outside the subgrid. As expected, the acceleration is systematically underestimated since the effective potential is softer than that of a point mass. Also as expected, the subgrid extends the range over which the force is accurate to within a few percent; the accuracy threshold (a little over 3% in this test) could be lowered by increasing the size of the subgrid, the spacing being equal.

Our second test checks that the accelerations computed on a set of adjacent subgrids agree with those one would obtain on a single, larger grid with the same spacing as the subgrids. We compare forces on individual particles randomly chosen to sample a uniform distribution. The long-range forces, which are adequately resolved on the parent grid, tend to cancel, so that the system is dominated by short-range interactions that will be most affected by the grid refinement. Our reference forces are from a non-subgridded run with 56^3 cells and 56^3 particles. We compare these to those obtained from three different runs with only 28^3 cells on the parent grid, in which all possible first-level subgrids are activated. The only difference between the three runs is in the width of the border region where adjacent subgrids overlap. The results are illustrated in figure 3. The magnitude of the force difference is plotted against that of the reference force for a randomly selected 1% of the particles (to avoid overcrowding the plot). Panels (a), (b), and (c) correspond respectively to a border width of 0, 1, and 2 parent grid cells. The solid diagonal line represents $|\delta\mathbf{F}|/|\mathbf{F}| = 0.1$; the last panel also contains a dotted line where $|\delta\mathbf{F}|/|\mathbf{F}| = 0.01$. The results show that when the border is sufficiently wide (at least two cells; we like to use three cells in production runs with larger grids), the forces computed by the subgrid method are mostly within 1% of the forces from a single grid of equivalent resolution. Whenever the border region is suppressed, an appreciable fraction of the particles exhibits force errors larger than 10%.

3.2. Collapse of a prolate ellipsoid

The collapse of a homogeneous self-gravitating pressure-less ellipsoid initially at rest can be described by a small set of coupled ordinary differential equations for the lengths of the principal axes, which can be integrated in a straightforward way (Lin, Mestel & Shu

1965). This solution provides a convenient test of our code. We followed the collapse of a homogeneous ellipsoid with a $2 : 1 : 1$ ratio between the lengths of the principal axes. The experiment was repeated for two different choices of the grid spacing in order to verify convergence towards the correct solution. For the higher resolution, we performed two runs, one using a single grid of 128^3 cells and one with a top-level grid of only 32^3 cells but up to two levels of subgrids. Each subgrid also has only 32^3 cells; when necessary, multiple adjacent subgrids were automatically generated by the code to cover the entire ellipsoid. The number of particles is the same in all three runs, about 10^5 .

Figure 4 shows the short axis c of the ellipsoid as a function of time t . The solid curve represents the analytic solution, the dot-dash curve the solution computed on the coarse grid, while the remaining two dashed curves show the results of the two high-resolution runs. The horizontal dotted line corresponds to the grid spacing in the high resolution runs; that of the low resolution grid is four times larger. Figure 5 presents a blown-up view of the same results around the time of collapse of the ellipsoid to a spindle.

One sees from these figures that increasing the resolution does indeed yield a better agreement between the N -body and analytic solutions. Furthermore, the results with subgridding are nearly identical to those obtained with a single grid of equivalent resolution. In the high-resolution runs, the minimum radius of the spindle is comparable to the grid spacing. At the lower resolution, it is significantly less than the grid spacing. We did not investigate the reasons for this in detail, but it is likely that the convergence is also affected by the number of particles used to represent the ellipsoid. In these tests we have kept this number constant.

The two runs without subgrids also used a small, constant value of the time step $\delta t = 0.001$. Collapse occurs after 1524 and 1644 steps respectively. The subgridded run, by contrast, used the Courant condition to adjust the time step; only 125 steps were required to reach the point of collapse. The good agreement between the high-resolution results obtained with both choices of time step confirms the validity of our implementation of adaptive time steps. We have also repeated the low-resolution run using our adaptive time step scheme; on figure 5 the results would be indistinguishable from those obtained with a fixed time step.

3.3. Secondary infall across a subgrid boundary

An interesting test of the behavior of mass flows into a subgrid is the case of accretion from a uniform-density background onto a point mass (or any other compact, spherically symmetric density profile). A regular lattice of 56^3 particles with zero initial peculiar velocity

was laid down in a computational box of unit side to be evolved with isolated boundary conditions in an $\Omega = 1$, $\Lambda = 0$ cosmological model. We added at the center of the box a single particle of mass $m = (4\pi/3)\rho_b \hat{x}_i^3 \hat{\delta}_i$, where ρ_b is the mean density of the other particles and of the external background, $\hat{x}_i = 0.1$, and $\hat{\delta}_i = 1$. We followed the collapse to a time $t_f = 1500t_i$, corresponding to an expansion factor $a_f/a_i = (t_f/t_i)^{2/3} = 131$.

A scaling solution is available (Gott 1975; Gunn 1977; Fillmore & Goldreich 1984; Bertschinger 1985): $\rho(r) \propto r^{-9/4}$. This simple law is expected to hold only for those shells that enclose a mass much larger than that of the initial seed and that have evolved for a few crossing times after their initial turnaround. The crossing time for a shell is of the same order as its turnaround time, and its proper radius is a factor $f \sim 0.5$ times the turnaround radius. Using a linear theory approximation (in which the density perturbation grows in place) until the turnaround at a mean enclosed overdensity $\bar{\delta} \simeq 1$, we find that for a given initial enclosed overdensity $\bar{\delta}_i$ the turnaround occurs at $a = a_i \bar{\delta}_i^{-1}$, the subsequent virialization at $a \sim 2a_i \bar{\delta}_i^{-1}$, and the final comoving radius of the shell is $f x_i (a_i/a_f) \bar{\delta}_i^{-1}$, where x_i is the initial comoving radius. Requiring $\bar{\delta}_i < 0.1$, only shells with $x_i > \hat{x}_i (\hat{\delta}_i/0.1)^{1/3} = 0.1 \times 10^{1/3} \simeq 0.215$ are expected to show self-similar behavior, and then only for $a/a_i \gtrsim 20$. One can also evaluate Bertschinger's (1985) equation (2.7) with $R_i = \hat{x}_i$, $\delta_i = \hat{\delta}_i$, $\tau = 1500$ (these values lead to $r_{\text{ta}}(t_f) = 0.237a(t_f)$) and make direct use of his numerically determined similarity solution.

A twist of our simulations is that shells with $x_i > 0.5$ are prevented from falling in by the fact that they are not entirely included within the simulation volume. Accordingly, the accretion will be starved for $\bar{\delta}_i \lesssim 10^{-2}$, and the last complete shell should virialize at $a/a_i \simeq 200$.

Our main reason for performing this test was to compare the solutions obtained with various treatments of the border region around a subgrid. We performed four runs: one with a uniform 64^3 grid, the other three with a 32^3 grid and a nested 32^3 subgrid with a linear refinement factor of 2. (After subtracting edge cells as discussed in § 2.4, the computational box was covered respectively by 56^3 and 28^3 cells.) In one run the border region was suppressed, as suggested by our tests with a bound clump crossing the boundary, while the other two both used a border width of two parent grid cells, once with the particles in the border region contributing to the subgrid potential without feeling its effects and once with the border particles being subjected to the subgrid potential without contributing to it. In the last two cases, the net effect of the force asymmetries on overdense regions results in an acceleration pointing respectively away from the subgrid and towards it.

Figure 6 shows the logarithmic density profiles for the runs we just described. The differences between the results of all these runs are minute; we find it difficult to ascribe any significance to such small deviations. This is reassuring: it suggests that the exact way

in which subgrid borders are treated does not unduly affect the profiles of collapsed peaks. The dotted line connects open triangles that correspond to the values given by Bertschinger (1985) in his Table 4. At small radii, his solution tends towards the expected $\rho \propto r^{-9/4}$, and ours is in good agreement with his. The first few caustics can easily be identified.

3.4. Expanding spherical void with compensating ridge

Peebles (1987; see also Peebles et al 1989, hereafter PMHJ) has proposed and used the following test for cosmological PM codes: integrating the evolution of a spherically symmetric under-dense region surrounding by a compensating over-dense shell. The interior of such a void expands faster than the universe as a whole, and in so doing compresses the surrounding shell, making its profile higher and narrower. The evolution can be computed analytically until the time at which the first density cusp appears. For Peebles' profile,

$$\delta(r) = -\delta_0 \left(1 - \frac{2}{3} \frac{r^2}{r_0^2}\right) e^{-r^2/r_0^2} \quad (32)$$

with $\delta_0 = 0.1$, this occurs at $a/a_i \simeq 120$ in a flat $\Omega = 1$ universe. (Here a_i is the initial value of the expansion factor a .) We integrated such a void, realized with 64^3 particles, on a 32^3 grid and compared our results to the analytic prediction at $a/a_i = 60$. Figure 7 can be directly compared to the corresponding figure 4 of PMHJ. A significant difference between our code and theirs lies in their use of a staggered grid for the force (Melott 1986). The staggered grid increases the spatial resolution twofold (which is why these authors used it) at the cost of inducing self-forces on the particles (for which reason we did not follow their example). Because of this difference, our results obtained with 64^3 particles on a 64^3 grid correspond to their results with the same number of particles on a 32^3 grid. A comparison reveals differences of detail, particularly in the structure of the outer parts of the shell, but our results match the analytic solution as closely as theirs.

We take this occasion to illustrate the energy conservation properties of the code. Figure 8 shows the evolution with time of the conserved quantities C and C' of equations 27 and 28 (top), as well as that of the ratio $|\Delta C|/|\Delta W|$ of the changes in C and in the total potential energy W from the start of the run (bottom). Apart from an initial transient due to rounding in the print-out from which the plot was made, an examination of the ratio shows the energy to be conserved to about 1–2% accuracy throughout the run.

4. Conclusions

We have developed a useful and versatile tool for the simulation of collisionless systems of gravitating particles. Our code is particularly suited to situations that call for both fine-grained mass resolution everywhere and high spatial resolution in selected regions of high density the exact locations of which need not be known in advance. Our method is a development of the well-known Particle-Mesh technique. Tests indicate that in comparable conditions our code performs substantially like similar codes described in the published literature. When subgrids are introduced to increase the spatial resolution locally, the results in the regions covered by the subgrids are in very good agreement with those of a conventional PM code with a single, finer grid. If the number of subgridded regions is sufficiently small, our approach requires less computing time and less memory than the equivalent single-grid approach. Furthermore, by not increasing the resolution in regions where the particle number density is low, we avoid making the behavior of the code collisional, which would be undesirable for applications to collisionless systems.

A significant advantage of PM (and its variants P^3M , AP^3M , etc.) for cosmological applications is that comoving coordinates and periodic boundary conditions can be supported in a natural way. However, periodic boundary conditions are not always a physically appropriate approximation. In particular, if one's interest is in systems not much smaller than the size of the computational cube, periodic boundary conditions introduce a much stronger coupling between the external tidal field and the internal dynamics of the system than one would expect to occur in the aperiodic real universe. Periodic boundary conditions are only appropriate when the individual structures of interest are much smaller than the computational volume, in which case the tides due to periodic images are small; but then the relatively small dynamic range of conventional PM methods severely limits the resolution that can be achieved. By introducing hierarchical subgrids, we are able to extend that dynamic range; however, it is also tempting to construct the simulation in such a way that the system of interest fills as much of the computational box as possible. This is what led us to implement isolated boundary conditions. In principle, the additional cost of imposing isolated boundary conditions (which is relatively small when hierarchical grids are used since isolated conditions have to be imposed on the subgrids in any case) is offset by the greater freedom one has to apply an arbitrary time-dependent external tidal field and to adopt a system of expanding coordinates that matches the evolution of the simulated object without necessarily coinciding with the expansion of the global cosmological model. Of course our method can also be used in a more conventional way, with periodic boundary conditions on the top grid; in fact, numerous simplifications occur when this is done. In addition, our code should be well-suited to non-cosmological dynamical simulations, *e.g.*, of brief interactions between already formed galaxies, star clusters, and so on.

Our approach also has a few limitations. The most important is shared by all particle simulation methods: it is generally impossible to improve the spatial resolution without a corresponding refinement of the time resolution: more time steps need to be taken. Other difficulties of note are the non-radial nature of forces at small separations (which could be cured, at some cost in computing time, by softening the interaction law and increasing the depth of subgridding to compensate for this softening), the complexity and difficulty of tuning the subgrid placement algorithm, and the fact that subgrids of fixed shape will almost inevitably also cover some regions where the particle number density is low. The behavior of the code can become collisional in such regions; this should not affect the computed structure of high-density condensations, but may well be a source of high-velocity particles that lead to shorter time steps according to the Courant condition. An enhancement to our current code could be to refrain from applying the refined forces to such low-density cells. Alternatively, it could prove useful to introduce individual time-varying softening lengths associated with individual particles, to represent the fact that particles in this method are to be thought of as possessing a finite extent that depends on the local number density. Another desirable improvement is the adoption of different time steps at different levels of grid refinement; the savings that can be achieved from this depend on the detailed structure of the tree of subgrids, and will be greatest for deep trees with most of their branches at the finer resolution levels.

This work was partially supported by grants NSF-AST-86-57647, NSF-AST-91-19475, and NASA-NAGW-2224. Some calculations were conducted using the resources of the Cornell Theory Center, which receives major funding from the U.S. National Science Foundation and the State of New York, with additional support from the Advanced Research Projects Agency, the National Center for Research Resources at the National Institutes of Health, IBM Corporation, and other members of the center's Corporate Partnership Program.

REFERENCES

Aarseth, S. J. 1985, in *Multiple Time Scales*, eds. Brackbill, J. U., Cohen, B. I. (Orlando: Academic), 377

Appel, A. W. 1981, Undergraduate thesis, Princeton University

Appel, A. W. 1985, *SIAM J. Sci. Stat. Comput.*, 6, 85

Anninos, P., Norman, M. L., & Clarke, D. A. 1994, *ApJ*, 436, 11 (ANC)

Barnes, J., & Hut, P. 1986, *Nature*, 324, 446

Bertschinger, E. 1985, ApJS, 58, 39

Bien, R., Fuchs, B., & Wielen, R. 1991, in Proceedings of the CP90 Europhysics Conference on Computational Physics, ed. Tenner, A. (Singapore: World Scientific), 3

Chan, K. L., Chau, W. Y., Jessop, C., & Jorgenson, M. 1986, in The Use of Supercomputers in Stellar Dynamics, eds. Hut, P., & McMillan, S. (Springer), 146

Couchman, H. M. P. 1991, ApJ, 368, L23

Dubinski, J. 1996, preprint astro-ph/9603097

Eastwood, J. W., & Brownrigg, D. R. K. 1979, J. Comp. Phys., 32, 24

Efstathiou, G., Davis, M., Frenk, C. S., & White, S. D. M. 1985, ApJS, 57, 241

Fillmore, J. A., & Goldreich, P. 1984, ApJ, 281, 1

Gelato, S., Chernoff, D. F., & Wasserman, I. 1994, in Numerical Simulations in Astrophysics, eds. Franco, J., Lizano, S., Aguilar, L., & Daltabuit, E. (Cambridge University Press), 85

Gelato, S. 1995, Ph.D. Thesis, Cornell University

Gelato, S., Chernoff, D. F., & Wasserman, I. 1996, in preparation

Gelb, J. M., & Bertschinger, E. 1994, ApJ, 436, 467

Gott, J. R. 1975, ApJ, 201, 296

Gunn, J. E. 1977, ApJ, 218, 592

Hockney, R. W., & Eastwood, J. W. 1981, Computer Simulation Using Particles (New York: McGraw-Hill) (HE)

Irvine, W. M. 1961, Ph.D. dissertation, Harvard University

James, R. A. 1977, J. Comp. Phys., 25, 71

James, R. A., & Weeks, T. 1986, in The Use of Supercomputers in Stellar Dynamics, eds. Hut, P., & McMillan, S. (Springer), 125

Jernigan, J. G., & Porter, D. H. 1989, ApJS, 71, 871

Jessop, C., Duncan, M., & Chau, W. Y. 1994, J. Comp. Phys., 115, 339 (JDC)

Layzer, D. 1963, *ApJ*, 138, 174

Lin, C. C., Mestel, L., & Shu, F. H. 1965, *ApJ*, 142, 1431

Melott, A. L. 1986, *Phys. Rev. Lett.*, 56, 1992

Peebles, P. J. E. 1987, *ApJ*, 317, 576

Peebles, P. J. E., Melott, A. L., Holmes, M. R., & Jiang, L. R. 1989, *ApJ*, 345, 108

Splinter, R. J. 1996, *MNRAS*, 281, 281

Suisalu, I., & Saar, E. 1995a, *MNRAS*, 274, 287

Suisalu, I., & Saar, E. 1995b, preprint astro-ph/9511120

Villumsen, J. V. 1989, *ApJS*, 71, 407

Xu, G. 1995, *ApJS*, 98, 355

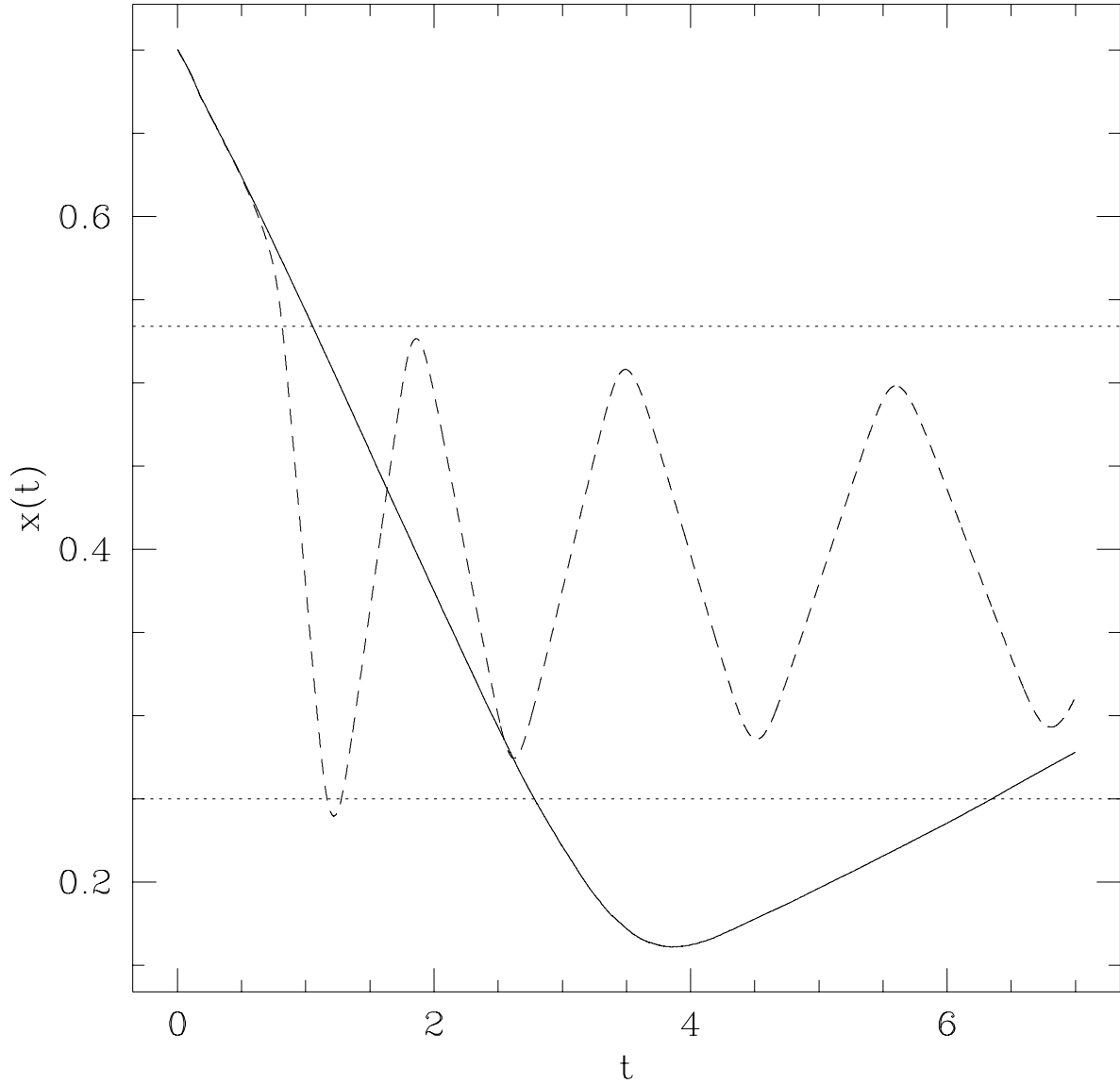


Fig. 1.— Trajectory of a bound clump crossing a fixed subgrid at normal incidence, (dashed curve) with and (solid curve) without using a buffer region two cells wide around the subgrid. The figure shows the projected position x of the center of mass as a function of time t . The horizontal dotted lines show the edges of the subgrid proper; the border region, when used, extends outwards by 0.07 units on both sides. The use of a buffer region is seen to produce significant unphysical changes in the total momentum of the clump.

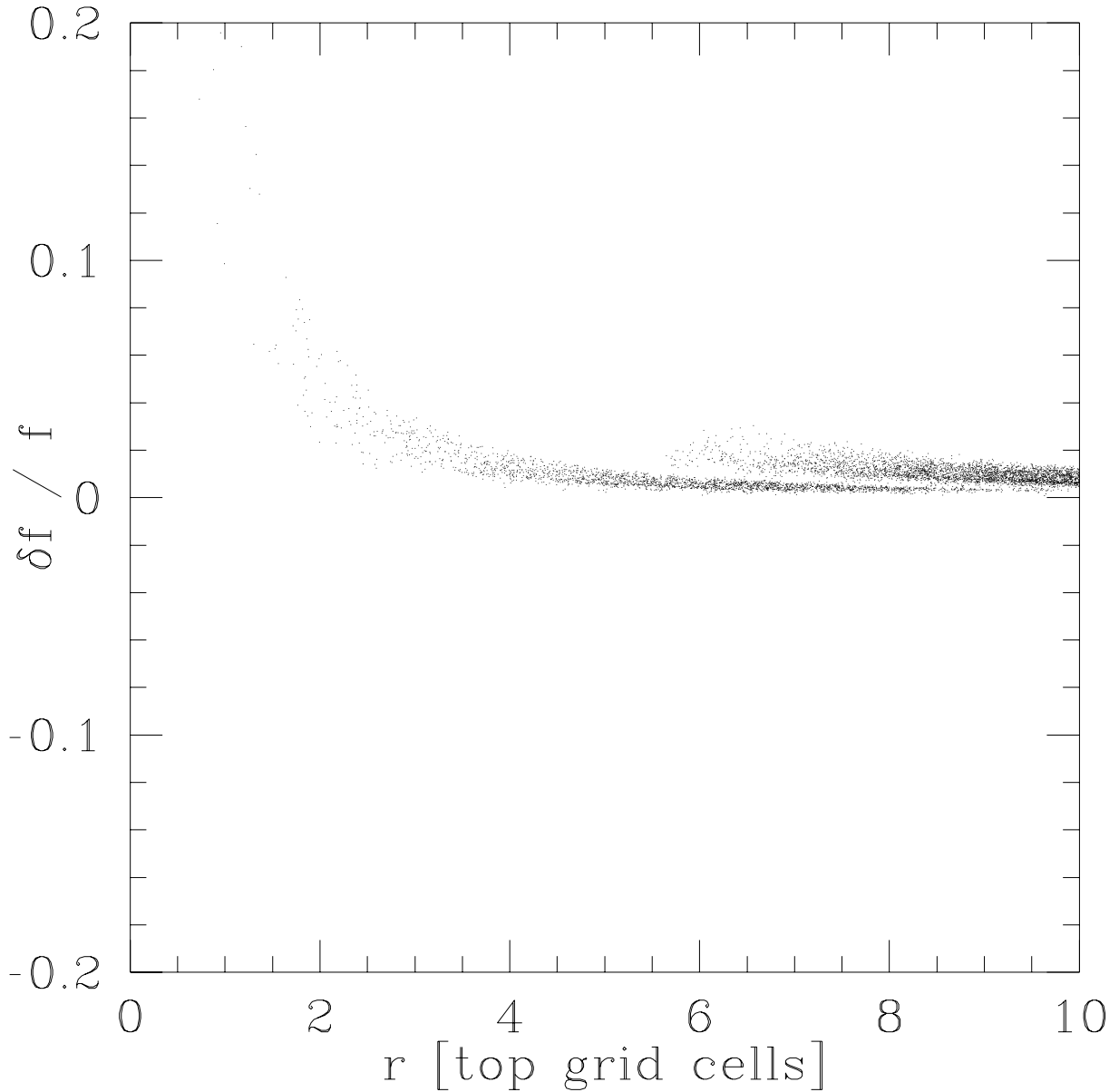


Fig. 2.— Relative error in the acceleration induced by a single massive particle on a number of massless test particles at various distances. The massive particle lies at the center of a subgrid whose spacing is half that of the top grid. The abscissa is measured in units of the top grid spacing; the ordinate is the relative error in the acceleration compared to the Coulomb formula. The error only reaches 10% for separations smaller than 1–1.5 cells (depending on the orientation of the separation vector); it is less than 4% outside the subgrid, a number that would be lower still if larger grid sizes had been used (this test was done with 32^3 nodes per grid). The two groups of points correspond respectively to test particles inside and outside the subgrid.

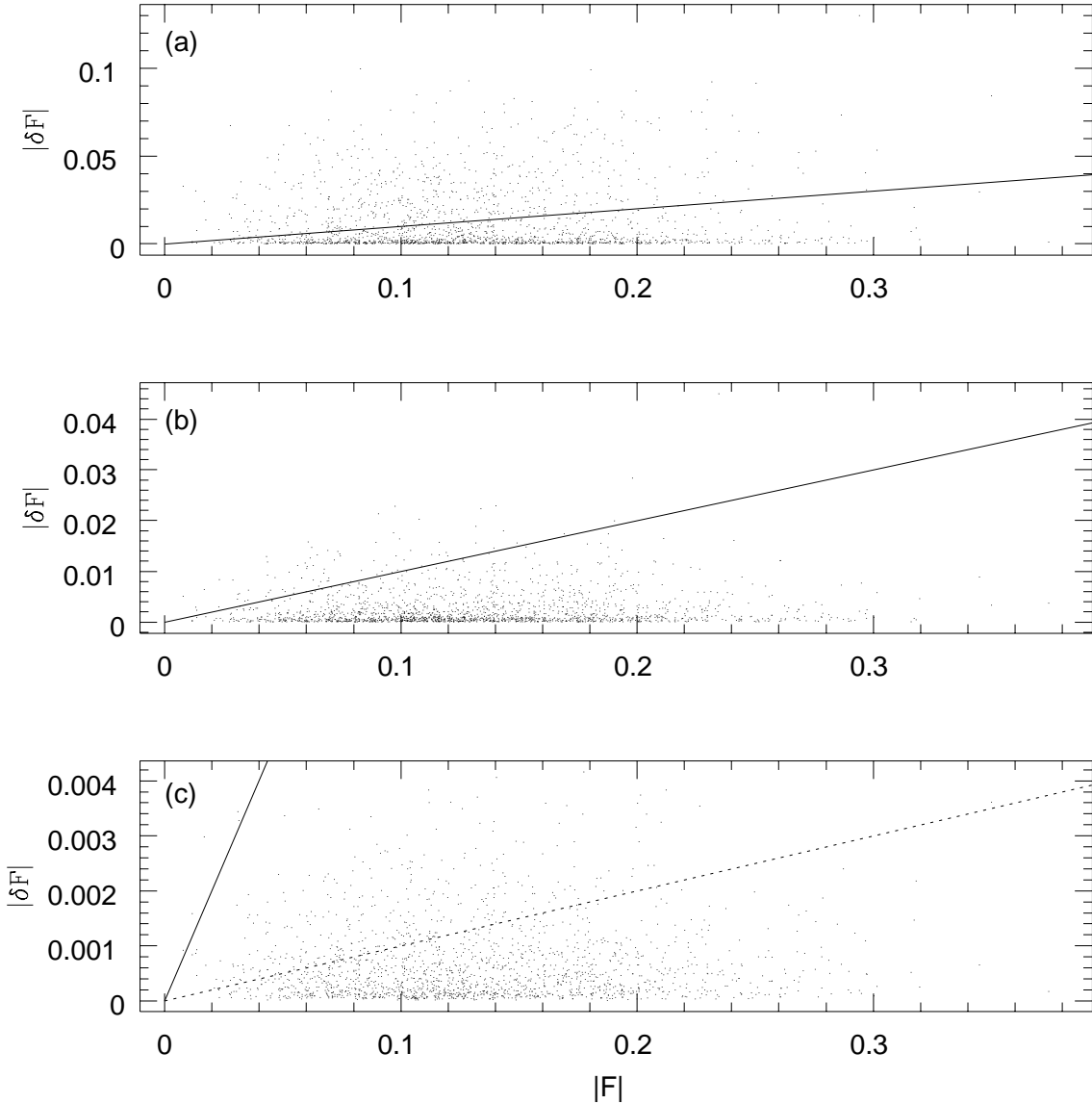


Fig. 3.— Comparison of the forces from the subgridding procedure with those from an equivalent single-grid PM code. The abscissa is the magnitude of the reference force, the ordinate the magnitude of the force difference (computed as a three-dimensional vector). Each point represents one particle; only a random selection of about 2000 particles is shown. The force differences depend on the width of the border region for overlap between adjacent subgrids. Panel (a) corresponds to a null width, panel (b) to a width of one cell, panel (c) to a width of two cells. The solid diagonal straight line shows where the force difference amounts to 10% of the force. In panel (c), a dotted line where the force difference is 1% is also plotted. One sees that when the border width is sufficiently large, the subgrid forces are substantially equivalent to those that would obtain from a single larger grid with the same spacing.

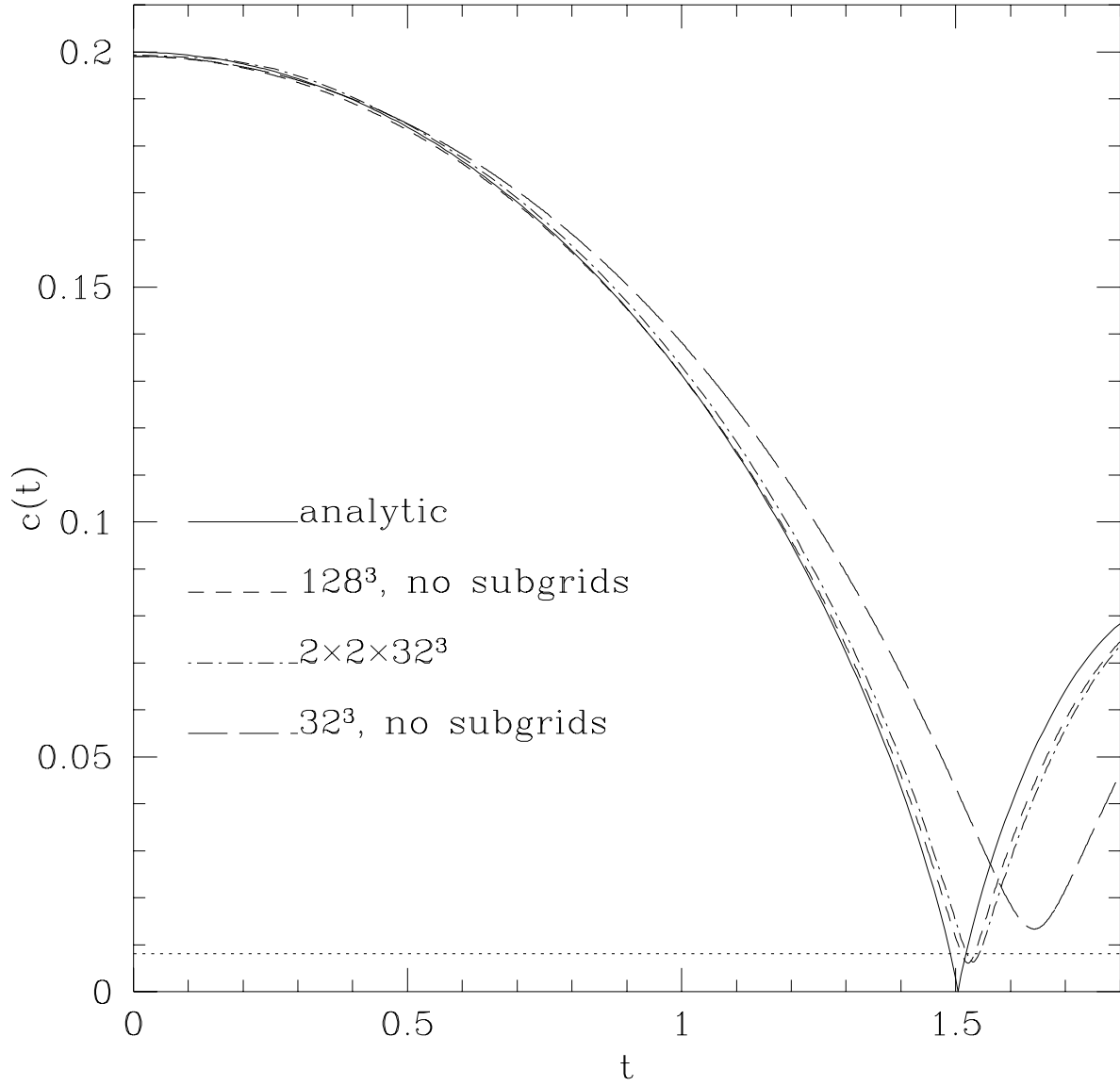


Fig. 4.— Minor axis $b = c$ of a collapsing prolate ellipsoid as a function of time. Solid curve: analytic solution. Long dashes: low-resolution (32^3 grid) PM simulation. Short dashes: high-resolution simulation (128^3 grid, no subgrids). Dot-dash curve: simulation with 32^3 base grids and two levels of subgrids, equivalent to the high-resolution simulation.

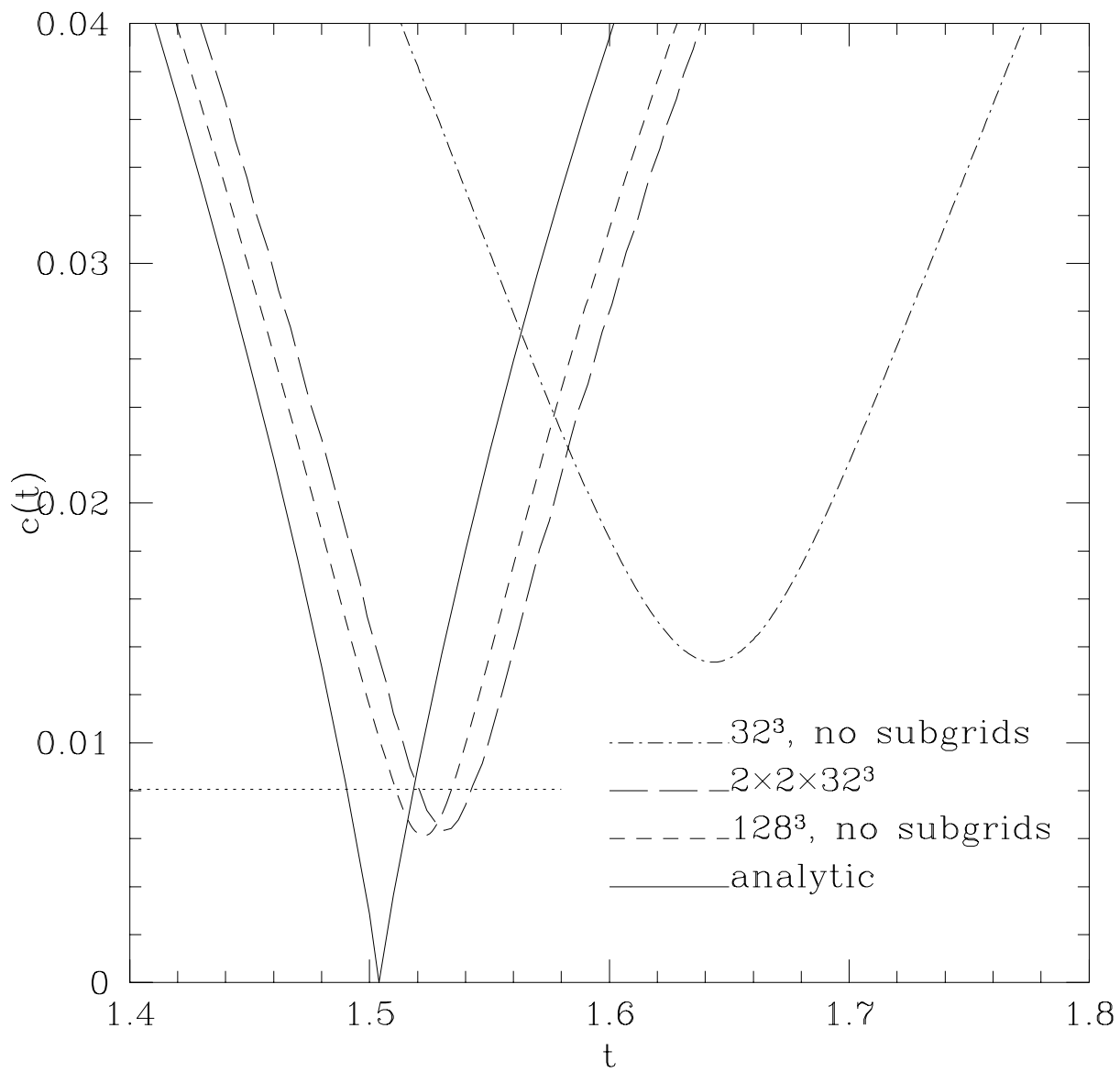


Fig. 5.— Enlarged view of figure 4.

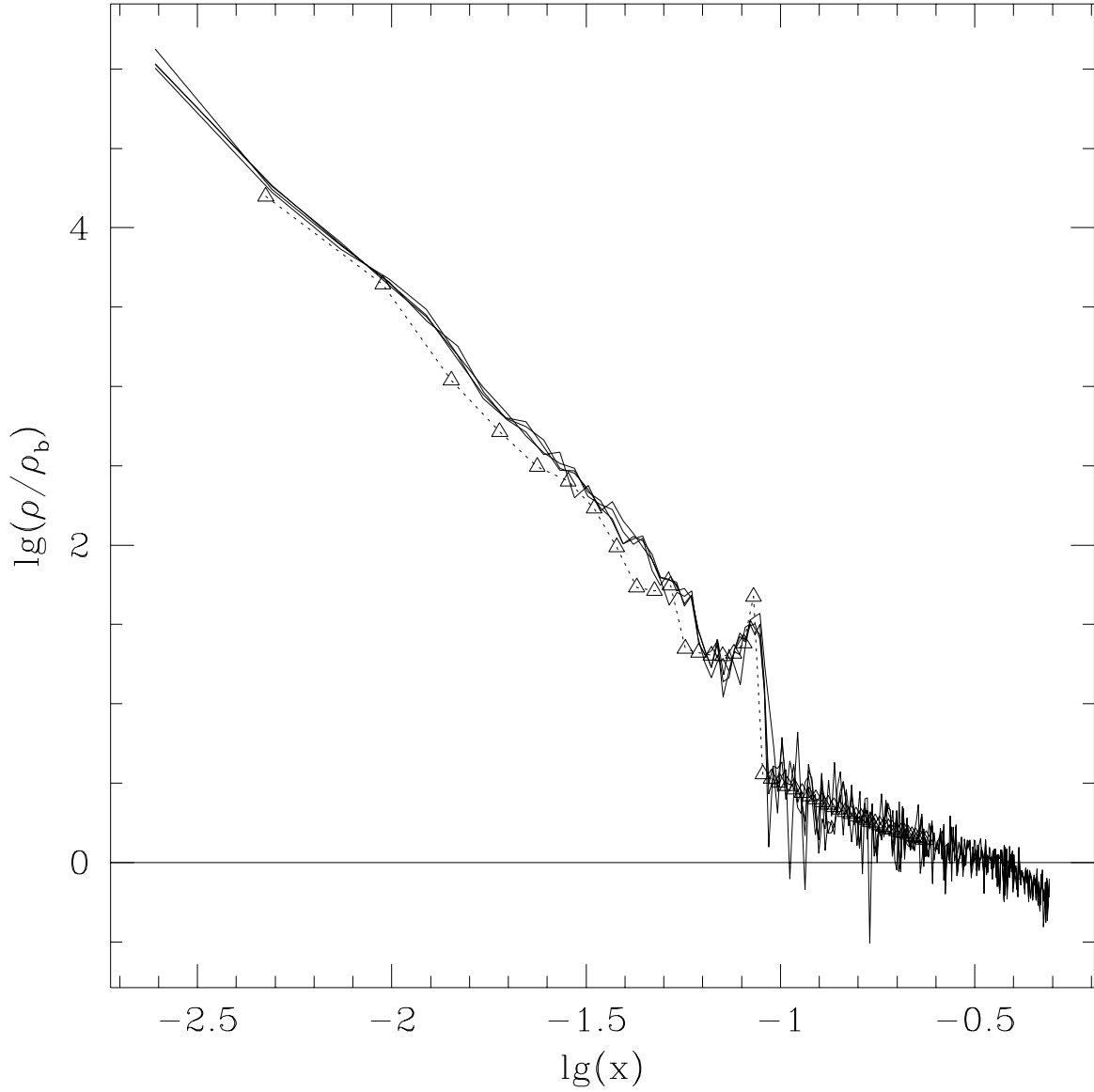


Fig. 6.— Radial density profile after spherical infall. The decimal logarithm of the density contrast $\delta = \rho/\rho_b$ is shown as a function of the logarithm of the comoving radius x , for simulations of a sharp peak accreting from a medium of uniform density ρ_b for an expansion factor $a_f/a_i = 131$ in a critical universe. The results of simulations realized with a single 64^3 grid and with a coarser 32^3 grid and one subgrid of equivalent resolution to the 64^3 grid are overlaid. The results are insensitive to the details of the treatment of particle flows through the subgrid boundary. The open triangles and the dotted line that connects them are from a table published by Bertschinger (1985), rescaled according to his prescriptions. The slope, the normalization, and the locations of the first few caustics are in good agreement.

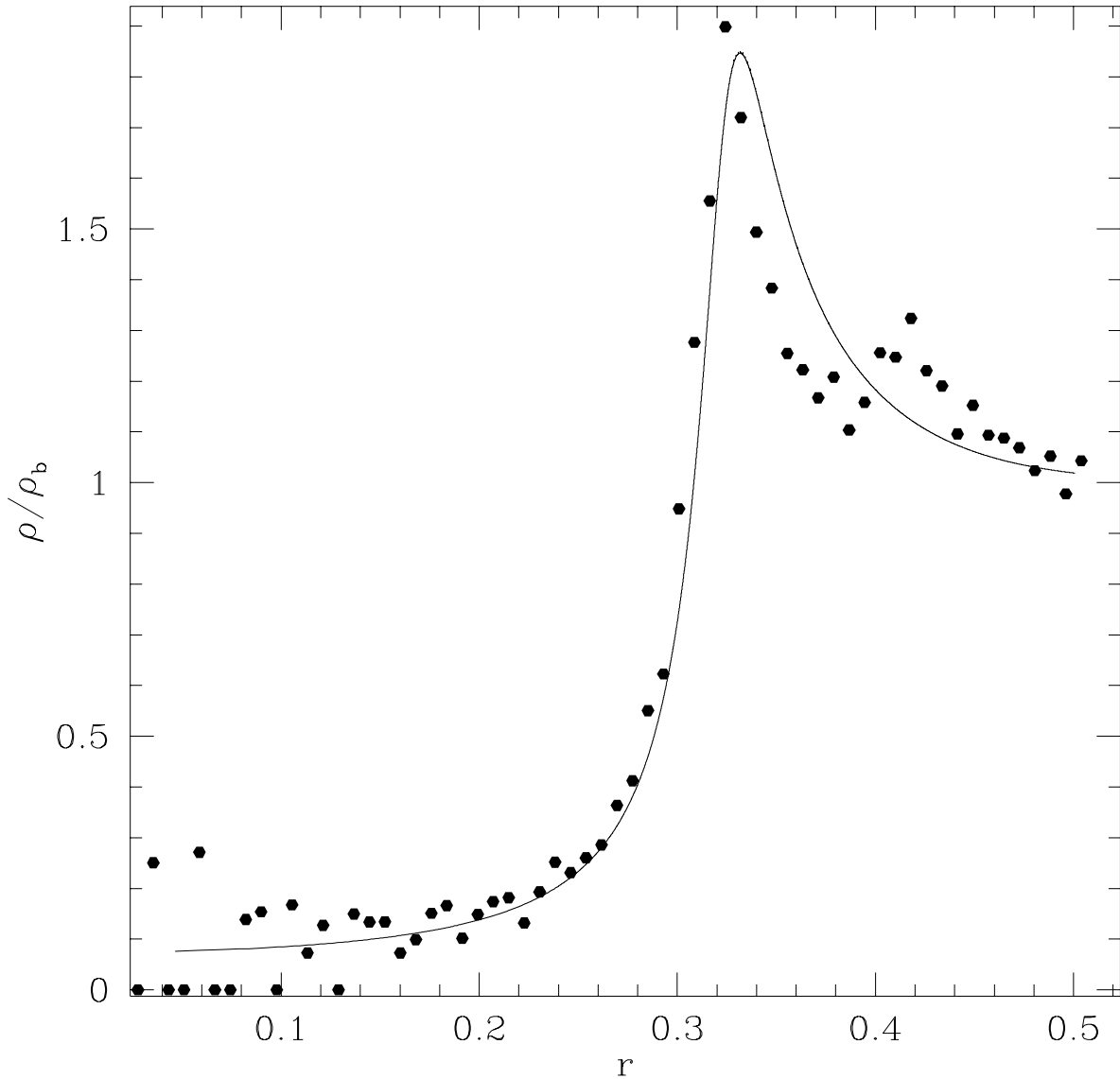


Fig. 7.— Result of evolving a spherical hole with a compensating ridge, as in Peebles (1987) and Peebles et al. (1989). The density contrast (ratio of the local value to the mean value for the cosmological model) is shown as a function of radial distance from the center of the hole. The curve is the analytic solution. Points show the mean density in equally spaced radial bins, obtained by running our code with a total of 64^3 particles and 64^3 grid cells.

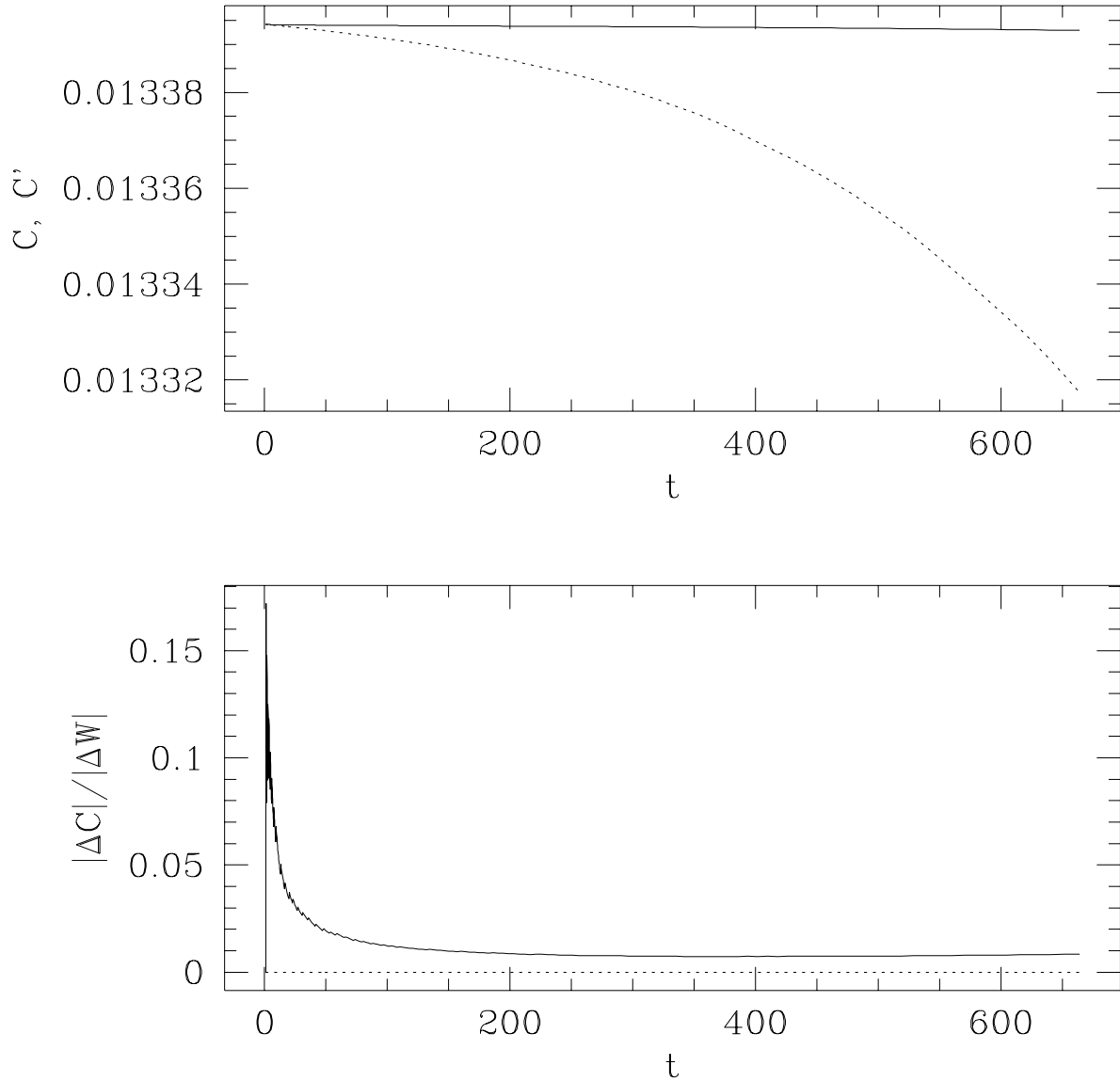


Fig. 8.— Energy conservation in the expanding void test. The top panel shows the evolution as a function of time ($t = 3/2(a/a_i)^{3/2}$) of the conserved quantities C (equation 27, solid curve) and C' (equation 28, dotted curve). The bottom panel compares the change in C , respectively C' , to that in W , respectively aW . The initial transient is imputable to the round-off one expects when both $|\Delta C|$ and $|\Delta W|$ are very small.